Journal of Power Sources 671 (2026) 239455

Contents lists available at ScienceDirect

Journal of Power Sources

journal homepage: www.elsevier.com/locate/jpowsour

Observing electrolyte motion in commercial cylindrical Li-ion cells using ultrasound imaging

Tobias Röhmel [a,b,c,*], Morian Sonnet [a,b,c], Gereon Stahl [a,b,c], Duc Minh Nguyen [a,b,c], Tim Falkenstein [a,b,c], Dirk Uwe Sauer [a,b,c,d]

[a] Chair for Electrochemical Energy Conversion and Storage Systems, Institute for Power Electronics and Electrical Drives (ISEA), RWTH Aachen University, Campus-Boulevard 89, Aachen, 52074, Germany
[b] Center for Ageing, Reliability and Lifetime Prediction for Electrochemical and Power Electronic Systems (CARL), RWTH Aachen University, Campus-Boulevard 89, Aachen, 52070, Germany
[c] Jülich Aachen Research Alliance, JARA-Energy, Templergraben 55, Aachen, 52056, Germany
[d] Helmholtz Institute Münster (HI MS), IMD-4, Forschungszentrum Jülich, Jülich, 52425, Germany

HIGHLIGHTS

- Novel ultrasound scanner for cylindrical Li-Ion batteries.
- First transmission images of cylindrical battery cells.
- Established correlation of Ultrasound intensity with electrolyte motion in cylindrical battery cells.

ARTICLE INFO

Keywords:
Ultrasound
Scanning acoustic microscopy
Cylindrical cell
26650
Electrolyte motion

ABSTRACT

Cylindrical Li-ion cells, increasingly adopted in electric vehicles, pose geometry-driven challenges for scanning acoustic microscopy (SAM). While SAM for flat cell formats is well established, spatial ultrasound imaging of cylindrical cells is under explored. We present a compact rotational ultrasound scanner that leverages cylindrical symmetry to generate two-dimensional angle–height images in both through-transmission and reflection using two opposing single-element transducers. To our knowledge, this is the first rotational ultrasound system that provides through-transmission imaging of cylindrical Li-ion cells and the first single-element reflection images that can be directly linked to large-scale internal structures such as current collector tabs. Early-time gating of the first arrival (through) and late gating of the first front-wall echo (reflection) suppresses circumferential and creeping waves, restoring interpretable contrast.

We validate the platform on aluminum reference dummies and demonstrate spatial imaging on three 26650 cells. The scanner produces interpretable angle–height maps in through-transmission and reflection that localize tabs, reveal orientation- and state-of-charge dependent electrolyte redistribution, and highlight stable attenuation features linked to internal mechanical conditions. Co-registration with X-ray CT provides a common angular frame and anchors acoustic contrasts in the underlying structure, establishing ultrasound as a practical complement to existing battery Non-destructive testing (NDT).

1. Introduction

Rechargeable lithium-ion batteries underpin modern electrified mobility, portable electronics, and grid-scale storage. As production volumes surge and performance requirements tighten, ensuring safety, reliability, and consistency across individual cells has become a central engineering challenge. Non-destructive testing (NDT) and imaging methods are therefore increasingly used to detect manufacturing defects, monitor evolving internal states, and inform design and process improvements without compromising cell integrity [1].

At the same time, there is a strong industrial trend towards large-format cylindrical cells, most prominently the 4680 form factor [2]. Multiple manufacturers, including Tesla, LG, BMW, and Panasonic, have announced or begun deploying large-format cylindrical cells for

* Corresponding author at: Chair for Electrochemical Energy Conversion and Storage Systems, Institute for Power Electronics and Electrical Drives (ISEA), RWTH Aachen University, Campus-Boulevard 89, Aachen, 52074, Germany.
E-mail address: batteries@isea.rwth-aachen.de (T. Röhmel).

https://doi.org/10.1016/j.jpowsour.2026.239455
Received 5 November 2025; Received in revised form 8 January 2026; Accepted 27 January 2026
Available online 7 February 2026

automotive applications [3–7]. The cylindrical format offers mechanical robustness, well-established winding and assembly processes, favorable pack-level thermal management strategies, and compatibility with structural battery concepts [8]. However, the wound jelly-roll architecture, curved metallic can, and internal tabbing present unique geometric and materials challenges for ultrasound-based NDT compared to pouch or prismatic cells. In particular, the cylindrical geometry imposes line-of-sight and incidence constraints, introduces complex wave paths and creeping waves along the can, and generates curvature-driven artifacts that complicate interpretation of ultrasound signals.

A broad suite of NDT modalities has been applied to Li-ion batteries, each illuminating complementary aspects of the internal state. X-ray computed tomography (CT) resolves internal geometry, defects, and heterogeneities with high spatial fidelity. Magnetic resonance imaging (MRI) and neutron imaging are sensitive to liquid-phase electrolyte and lithium distributions, revealing transport and compositional changes during operation [9–11]. Infrared thermography captures dynamic thermal signatures that correlate with internal resistive losses and structural faults [12,13]. Ultrasound, including scanning acoustic microscopy (SAM), has been used successfully for defect inspection and lithium plating detection, especially in pouch and prismatic cells where flat geometries are amenable to linear scans [14–16]. Each technique entails trade-offs in cost, throughput, spatial/temporal resolution, and the specific physical contrast it exploits. Ultrasound is particularly attractive because the instrumentation is comparatively inexpensive and compact, measurements are fast, and the method is non-ionizing, avoiding toxic radiation and shielding requirements.

Within ultrasound-based battery diagnostics, a substantial literature exists on cylindrical cells, but it focuses almost exclusively on point measurements for state estimation rather than spatial imaging. Numerous studies report temperature tracking, state-of-charge (SoC) inference, and state-of-health (SoH) assessment from ultrasonic travel time, attenuation, and spectral features acquired at one or a few fixed positions on the cell [17–21]. Advanced signal processing and excitation schemes, ranging from feature engineering to machine learning and modern AI approaches, have been used to map ultrasound observables to SoC/SoH and to classify degradation modes [22–24]. In parallel, modeling and simulation efforts have deepened the physical understanding of ultrasound propagation in layered electrode stacks, current collectors, separators, and electrolyte-filled pores, clarifying the roles of frequency-dependent attenuation and scattering in complex battery materials [25–29]. For pouch and prismatic cells, SAM-like linear scans are widely used to obtain spatially resolved images of near-surface defects and local plating [15,16].

Despite this progress, spatially resolved ultrasound imaging of cylindrical cells remains largely unexplored. To our knowledge, only one prior work demonstrates image formation on cylindrical cells using a phased array in reflection mode [19]. Phased arrays allow electronic steering and focusing, but reflection-only imaging is inherently biased towards the near-surface region in cylindrical geometries, and the hardware complexity and cost can be prohibitive for routine or in-line screening. Moreover, existing single-element studies on cylindrical cells rely on measurements at a single circumferential position and height. This neglects the strong angular and axial heterogeneity introduced by tabs, local mechanical constraints, and non-uniform electrolyte distribution. As a consequence, conventional point measurements may miss or misinterpret spatially localized phenomena, and the influence of measurement location on inferred SoC/SoH remains largely unquantified.

A particularly important example of such spatial heterogeneity is electrolyte redistribution. Volume changes of the active materials upon (de)lithiation modify the pore volume of the porous electrodes and separators, expelling or drawing in electrolyte as a function of SoC [30]. In wound cylindrical geometries, this can lead to gravity- and capillarity-driven accumulation of liquid electrolyte in the central mandrel region. Ultrasound is naturally sensitive to these changes because acoustic impedance $Z = \rho c$ and attenuation depend on the local distribution liquid electrolyte and potential voids [31]. Redistribution of electrolyte alters both the effective acoustic path and the local impedance and attenuation along that path, so that the amplitude and spectral content of transmitted and reflected waves encode information about electrolyte-filled versus depleted regions. However, prior ultrasound studies on cylindrical cells have not provided spatial maps that directly link acoustic contrast to electrolyte motion.

This paper addresses these gaps by introducing a compact rotational ultrasound scanner tailored to cylindrical Li-ion cells that enables combined through-transmission and reflection imaging. Two opposing single-element transducers are fixed in space while the cell is rotated, leveraging cylindrical symmetry to generate unrolled angle–height images of the can and jelly roll. Early-time gating of the first arrival in through-transmission suppresses circumferential and creeping waves, yielding interpretable line-of-sight attenuation maps. Late gating of the first front-wall echo in reflection isolates near-surface information and enhances sensitivity to large-scale structures at the can wall, such as tabs. Compared to prior single-point single-element measurements, our system provides full circumferential coverage and reveals how the measurement location affects the observed ultrasonic response. Compared to phased-array approaches, it achieves spatial imaging with much simpler and lower-cost hardware, and it is the first, to our knowledge, to demonstrate through-transmission imaging of cylindrical cells and to correlate both transmission and reflection contrasts with large-scale internal structures.

The main objectives and contributions of this work are:

- We develop an open-hardware rotational ultrasound scanner for cylindrical Li-ion cells that produces two-dimensional angle–height images in both through-transmission and reflection using two opposing single-element transducers.
- We identify the technical limitations that curvature and cylindrical geometry impose on ultrasound imaging and demonstrate that appropriate time gating of the first arrival (transmission) and of the late front-wall echo (reflection) restores interpretable spatial contrast.
- We show, for the first time, that reflection-mode images of cylindrical cells can be co-registered with X-ray CT to localize tabs as large-scale angular sectors, thereby linking ultrasound contrast to a specific structural feature of the jelly roll.
- We demonstrate that through-transmission images are sensitive to orientation- and SoC-dependent electrolyte redistribution

2. Experimental

2.1. Custom ultrasound scanner for cylindrical cells

A novel, custom-designed ultrasound scanning system, depicted in Fig. 1, was developed specifically for cylindrical Li-ion battery cells. The design is available as open hardware in our Git repository [32]. Unlike conventional scanners optimized for pouch or prismatic cells, which typically translate the transducers linearly across the cell surface, the unique geometry of cylindrical cells enables rotational scanning by rotating the cell, rather than the transducers. This approach enables circumferential inspection without requiring repositioning of the transducers.

Rotating the cell instead of the sensors was chosen deliberately for mechanical and electrical reasons. A scanner that rotates the transducers around a stationary cell would require a mechanically larger rotating frame, which is more susceptible to wobble and misalignment and thus to angle-dependent changes in coupling and signal amplitude. In addition, the transducer cables would need to be routed through the rotating structure, which introduces cable motion as a noise source, complicates shielding against electromagnetic interference, and practically limits the number of possible revolutions. By contrast, keeping the

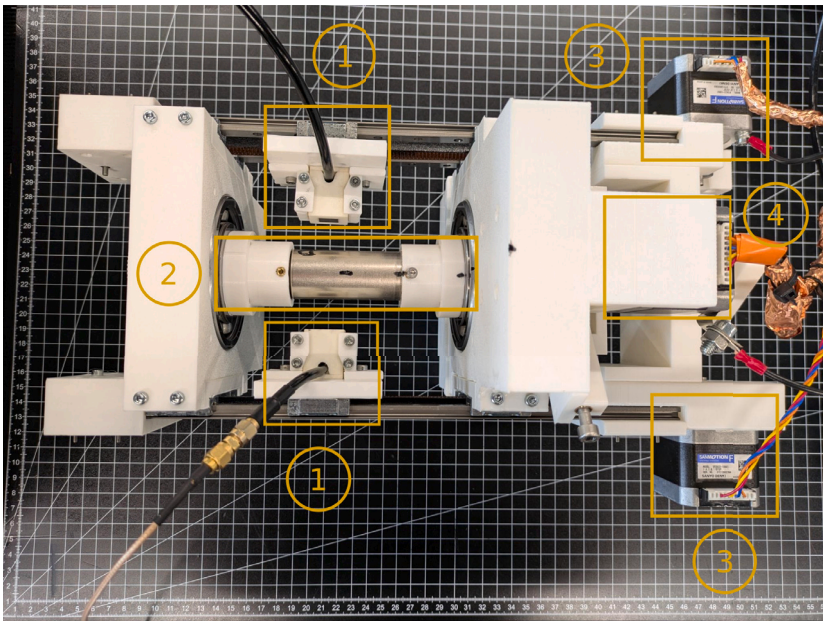

Fig. 1. Overview of cylindrical cell ultrasound scanner. **(1):** Transducers on linear axis. **(2):** Cell clamped on rotation axis. **(3):** Motors for linear motion. **(4):** Motor for rotation.

transducers fixed on a rigid frame and rotating only the comparatively small cell allows a more compact, stiff design, avoids cable twisting or entanglement, and enables reproducible rotations over many cycles. A rotational scan also ensures that all image lines are acquired with the same rotation direction, avoiding the line-to-line reversal that can cause subtle row shifts in conventional raster (x–y) scans.

To ensure high measurement fidelity and repeatability, particular attention was given to securing positioning and clamping within the setup. The fixture was engineered to hold the cell such that its longitudinal axis coincided with the rotation axis of the scanner. Any deviation or wobble in the cell's position introduces artifacts in sensor readings due to variable relative positioning during rotation.

The custom ultrasound scanner was constructed using three stepper motors, each precisely controlled via a 3D printer mainboard (BTT SKR 3). The board operates with a modified Marlin firmware, enabling tight synchronization between mechanical movements and the generation of ultrasound pulses [33]. The system features a single rotational axis dedicated to rotating the cylindrical cell about its central axis, allowing for full circumferential scanning. Additionally, two independent linear axes permit vertical translation of two opposite transducers along the height of the cell. Using separate motors for the two length axes keeps the mechanical design simple and simplifies the assembly.

The spacing between the opposing transducers was chosen such that, in addition to the 26650 format studied here, larger cell geometries can also be investigated in the same setup. In particular, the transducer distance and travel range accommodate the diameter and length of large-format cylindrical cells such as 4680, providing a path towards scaling the method to industry-relevant formats without redesigning the mechanical structure. Motor cables were shielded to mitigate the influence of electromagnetic interference (EMI) on the measurement.

To ensure precise alignment and repeatability across all scans, all motion components are mounted on linear rails. This rigid construction maintains consistent geometry between the transducers and the sample during both rotation and translation.

All transducers were custom-fabricated following the methods described in [16] and have a primary frequency of 1 MHz while the second mode is at 200 kHz. From the perspective of scanning acoustic microscopy, where center frequencies of 5–50 MHz are common, 1 MHz already represents a comparatively low-frequency choice. We deliberately selected these transducers because they are the lowest-frequency elements available to us and therefore provide the best compromise between penetration and resolution for through-transmission across the full thickness of a cylindrical cell. Attenuation and scattering in the porous electrode stack and separator increase strongly with frequency, so higher-frequency components are rapidly damped when traversing the wound jelly roll. Using the lowest available frequency maximizes the detectable signal on the opposite side of the cell and ensures sufficient signal-to-noise ratio for through-transmission imaging. As a consequence, while the electrical excitation is matched to the 1 MHz resonance, the cell effectively acts as a strong high-pass filter for attenuation: the higher-frequency content is preferentially suppressed, and the waveform arriving at the receiving transducer is dominated by energy around the second mechanical resonance near 200 kHz, as observed in the measured spectra. This is consistent with our imaging objectives. The aim of the present work is not to resolve microscopic defects, but to obtain robust, bulk-sensitive contrast associated with large-scale structures such as current collector tabs and macroscopic electrolyte redistribution. For these targets, penetration and sensitivity to integrated line-of-sight properties are more critical than maximizing spatial resolution, and a low effective frequency content is well aligned with that goal. The signal response and frequency spectrum of the ultrasound signal traveling just through the silicone oil is shown in supplemental Figs. 4–6, where the response is also compared to the signal and spectrum that is received after the signal travels through a cell. . The 400 V ultrasound excitation pulses were generated by an Olympus 5077PR, while the received signals were digitized using a PicoScope 5554D oscilloscope with a sampling frequency of 125 MHz. No analog amplification was applied. All aspects of scanner operation were managed through custom software developed in Rust. This setup, in combination with the custom software, enables the collection of reflection and through-transmission measurements simultaneously by capturing data on two oscilloscope channels. All tests were conducted in a container filled with silicone oil, providing good acoustic coupling and electrical isolation, and in a temperature-controlled room at ca. 22 °C. No active circulation or pumping took place during data acquisition, so there is no externally driven flow field in the bath.

The robustness of the mechanical scanning process was assessed through repeatability studies, in which identical scans were repeated

on the same cell without changing the setup (see Supplementary Figures S7–S8). Pixel-wise comparison of repeated images shows that the mean percentage difference in gated through-transmission intensity is ≈4.8% (median 0.8%), while for reflection the mean percentage difference is ≈0.6% (median 0.3%). The largest differences cluster on the top first 2 mm of the images were the cell overlaps with the clamping structure. The very low median difference indicates that residual influences such as minor fluid motion, motor micro-vibrations, or environmental perturbations act effectively as random noise rather than as systematic artefacts that could mimic the large-scale features discussed in the Results. Consequently, the reproducible, structured contrasts observed in the main angle–height images (e.g., tab sectors and electrolyte-related bands) can be attributed to the cell under test rather than to instabilities of the scanning process.

2.2. Ultrasound scanning background

This subsection summarizes the core relations used in our analysis. The acoustic impedance Z of a medium is

$$Z = \rho c,$$

with mass density ρ and sound speed c. When a plane acoustic wave reaches an interface between two media with impedances Z_1 and Z_2, part of the wave is reflected back and part is transmitted into the second medium, and the relative amplitudes depend on the contrast between Z_1 and Z_2. At normal incidence the pressure reflection R and transmission T coefficients for an interface from Z_1 to Z_2 are

$$R = \frac{Z_2 - Z_1}{Z_2 + Z_1} \tag{1}$$

$$T = \frac{2Z_2}{Z_1 + Z_2} \tag{2}$$

For image formation, the intensity within a selected time gate is computed as the windowed energy of the received signal

$$I_{\text{gate}} = \int_{t_0}^{t_1} s(t)^2 \, dt \tag{3}$$

where $s(t)$ is the measured waveform and $[t_0, t_1]$ is the analysis time window aligned to the arrival of interest. Reflection measurements are governed by impedance contrasts at interfaces and therefore emphasize boundaries and near-surface structure. Transmission measurements are governed by the portion of the wave that passes through the specimen and therefore emphasize bulk properties along the path, integrating attenuation, scattering, and velocity changes across layers. Short time gates isolate the desired arrivals and reduce contributions from later, multiply reflected or surface-guided energy, improving interpretability in both modes.

2.3. Cell specifications

In this study, three new Keeppower UH2652 26650 cylindrical cells were used, each rated at 5200 mAh with a nominal voltage of 3.7 V, a charge voltage of 4.20 V, and a discharge cut-off of 2.50 V. The 26650 format was chosen as a compromise between industry-relevant larger cells that provide a greater scanning circumference and the need for smaller diameters to ensure a sufficiently strong through-transmission ultrasound signal. The exact chemistry of the cells is unknown, but the voltage profile of a standard charge, shown in supplemental Figure S3, suggests an NMC chemistry.

2.4. CT acquisition parameters

Computed tomography (CT) was performed on a Zeiss METROTOM 800 225 kV system. A copper prefilter of 0.75 mm, tube voltage 215 kV, tube current 416 µA, integration time 267 ms, and an amplifier gain of 2x were deployed, resulting in a voxel size of $(52.5\ \mu\text{m})^3$. These settings provided sufficient contrast to resolve the center hole, tab features near the can wall, and gross electrolyte distributions, while allowing for the scanning of a complete cell in one CT measurement.

To establish a common angular reference between CT and ultrasound, a thin copper strip was affixed to the can to serve as a high-contrast orientation marker in the CT volume. Corresponding alignment markings were drawn onto the cells, so that the angular zero used in the unrolled ultrasound images could be reliably mapped onto the horizontal CT cross-sections.

For the ultrasound scans, the marked angular position was aligned by hand such that the pencil mark faced upwards in the scanner, defining the 0° direction of the unrolled angle–height images. This procedure introduces the main sources of registration uncertainty: manual angular placement of the marker relative to the scanner reference, and (ii) small residual misalignments of the cell within the clamp.

To investigate the possibility of a gap between jelly roll and can, we inspected the reconstructed CT volumes for a continuous low-density ring at the can–jelly roll interface. At the achieved voxel size, no such feature was observed for any cell or orientation. Post-mortem opening likewise revealed no free annulus. From an acoustic standpoint, a gas or vacuum gap would create a severe impedance mismatch at the can wall and largely suppress the early through-transmission used here. The robust first-arrival signals across angles and heights are therefore incompatible with such decoupling, indicating that the electrolyte-related contrasts reported here are not confounded by a can–jelly roll gap.

Representative vertical CT slices for one cell at two states of charge (SoC) are shown in Fig. 2. Panel (a) depicts the 4.2 V condition with the negative tab facing downwards relative to gravity, panel (b) shows 4.2 V with the positive tab down, and panel (c) shows 3.5 V. In both 4.2 V orientations, the central center hole exhibits a distinct contrast consistent with liquid electrolyte being present in the middle hole. This effect is highlighted by a red ellipse. In contrast, at 3.5 V, the center region shows no such electrolyte signature. This electrolyte motion is caused by volume changes in the active material, which alter the available pore volume [30].

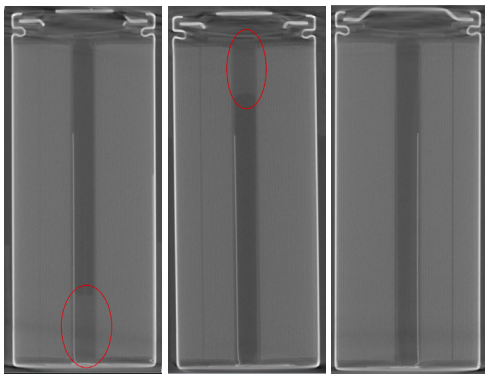

Fig. 2. CT images show bulk electrolyte movement in a fully charged cell. No bulk electrolyte visible at 3.5 V. **(a):** Cell at 4.2 V, negative tab facing down. **(b):** Cell at 4.2 V, positive tab facing down. **(c):** Cell at 3.5 V, negative tab facing down.

2.5. Reference data generation

To visualize the internal structure of cylindrical Li-ion cells, a two-dimensional (2D) ultrasound image is generated by systematically acquiring measurements as the cell is rotated and scanned along

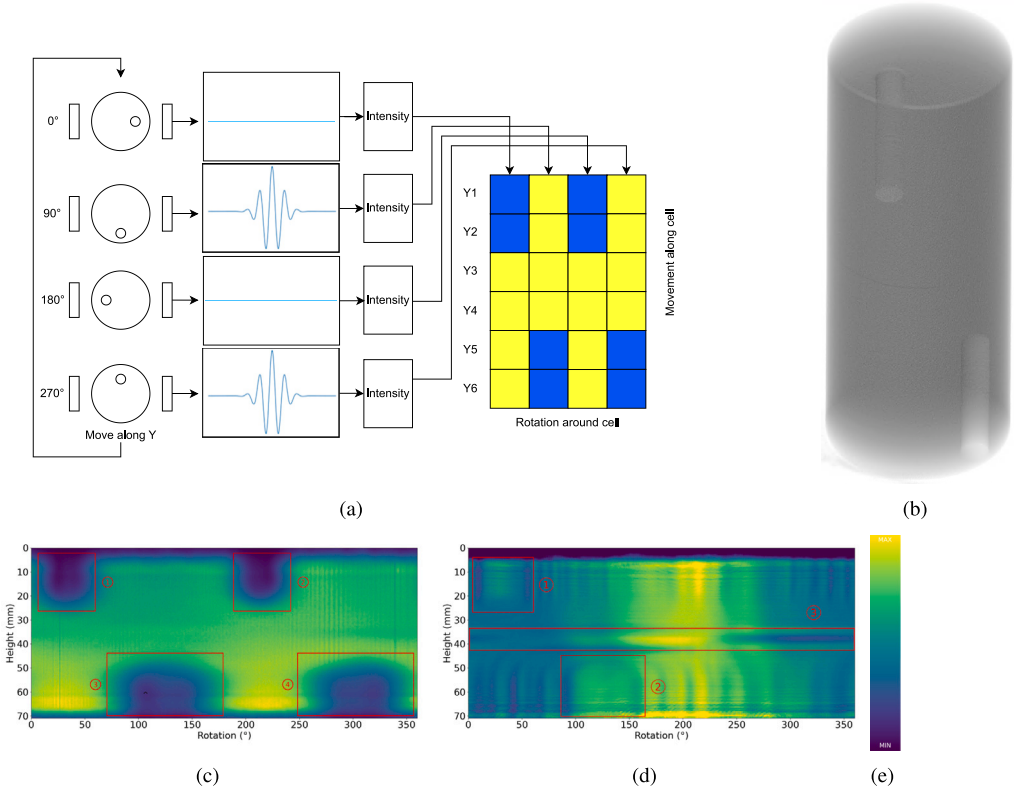

Fig. 3. Image generation from scanning data and results from reference scans. **(a):** Schematic representation of how individual ultrasound measurements get mapped to image pixels. **(b):** CT image of aluminum reference dummy. **(c):** Through transmission image of aluminum reference dummy. Markings 1 and 2 identify low-intensity sectors from intersections with the hole near the outer surface, while markings 3 and 4 identify low-intensity sectors from intersections with the hole closer to the cylinder center. **(d):** Reflection image of aluminum reference dummy. Markings 1 and 2 identify regions were the reflection beam intersects with the two holes. Marking 3 identifies a workpiece artifact that results from re-chucking in the lathe. **(e):** The viridis color scale used to assign colors to intensity values.

its length. To validate the measurement process, a reference dummy cell was constructed from a solid aluminum cylinder with two off-axis holes positioned at a 90° angular offset. These features provide well-defined landmarks for validating scanner performance and image reconstruction.

The imaging sequence begins by securely mounting the scan object in the scanner to ensure precise alignment with the rotation axis. The cell is then rotated through a full 360°, with ultrasound pulses triggered at predefined angular intervals (e.g., every 1° or as required for resolution). At each angular position, an ultrasound pulse is transmitted through the cell, and the transmitted and the reflected signals are recorded.

After completing one full rotation at a fixed height along the object, both transmitting and receiving transducers are synchronously moved to a new vertical position along the length of the object. This process, which involves rotating through 360° while acquiring measurements at each step, is repeated across multiple heights until data have been collected over the entire active region of interest.

The acquired dataset can be visualized as a 2D image, where each pixel corresponds to an individual measurement. In this representation, the x-axis represents the rotational angle (0–360°), while the y-axis denotes the vertical positions along the length of the object. The pixel color is calculated by taking the intensity of the measurement at the respective position and mapping it to a color using the scale shown in Fig. 3 panel (e). Features within the cell, such as off-axis holes in reference dummies, appear as distinct intensity variations in specific locations on this map, corresponding to their angular and axial positions.

The image generation process is visualized in Fig. 3 panel (a) with the example of the aluminum reference dummy. A slice at Y1 of the dummy at different rotation angles is shown on the left. Note that the transducers are stationary during the cell rotation. In this example, measurements are taken at 90° intervals and the resulting timeseries of the through measurements are shown. When the transducers are aligned with a hole, the transmitted signal intensity is very low, which results in a blue pixel. When only aluminum and no hole is between the transducers, the transmitted intensity is high, which results in a yellow pixel. Since a 180° rotation of the cell results in the same transmission path but with the transmitter and receiver swapped, the generated images exhibit a repeating pattern, where the left and right halves of an image appear very similar. Once a full rotation is completed, the transducers are moved one step along the length of the dummy, and another rotation with the corresponding measurements takes place. For the aluminum dummy, the first third of the image shows the hole that intersects the transmission path twice. The middle third has no obstructions and is uniformly yellow. The last third shows the second hole that is shifted 90° with respect to the first.

Reflection images are generated in the same manner, but do not show the repeating pattern because the sound wave penetrates only into the surface of the object before being reflected. All images shown in this work have 360 measurements per full rotation, and y increments occur in 0.5 mm steps over a scan area of 74 mm, resulting in an image size of 360x148.

In Fig. 3, panel (b) shows a CT 3D image of the aluminum dummy with the two off-axis holes, panel (c) is the corresponding through-transmission image, and panel (d) is the reflection image.

Because of the cylindrical geometry, through-transmission images become difficult to interpret if the intensity is computed over the entire received waveform. Multiple internal reflections and circumferential

(around-the-can) paths dominate the envelope, obscuring true line-of-sight attenuation. Restricting the evaluation to a short gate using $[t_0, t_1]$ in Eq. (3) at the start of the signal mitigates these effects. This start-of-signal window removes the late parts of the waveform that come from internal echoes. It emphasizes the first arrival that travels straight through the cell and de-emphasizes slower energy that runs along the curved can or takes longer routes around the circumference. With the direct path dominating, the intensity reflects true line-of-sight transmission and the unrolled images recover the expected 180° symmetry.

Consistent with the geometry, the through-transmission image (Fig. 3c) exhibits dark indications when the straight path aligns with one of the holes. The indications associated with the hole closer to the cylinder center (Marking 3 and 4) are slightly broader than the band from the hole nearer the outer edge (Marking 1 and 2). This is expected because, over a full rotation, the direct through path intersects a larger effective arc of the inner hole than of the near-edge hole, leading to a broader angular sector of reduced transmission.

The reflection image (Fig. 3d) does not show a 180° symmetry because the interrogating wave only penetrates into the near-surface region before being reflected. The measurement is therefore inherently one-sided. As in through-transmission, the feature from the hole closer to the surface (Marking 1) is narrower, since the wavefront interacts with it over a shorter arc-length. Unlike through transmission, the reflection image shows baseline or even increased intensity when a hole is directly aligned with the sensor, whereas attenuation occurs when rotation places a hole edge within the beam footprint, where partial interception and scattering reduce the reflected signal. The hole indications are surrounded by regularly spaced dark and bright bands that point to a more complex wave interference around the holes. Additionally, panel (d) contains alternating dark and bright features (Marking 4) near the mid-height of the image that are not related to internal holes. These arise from a small manufacturing artifact of the dummy. During turning on the lathe, the workpiece was re-chucked, and a slight misalignment between the first and second rotation axes introduced a tiny circumferential step (less than 0.2 mm) at mid-height. This subtle geometric discontinuity alters the reflected amplitude, resulting in the observed contrast at the center of the reflection map.

The first rows in the unrolled ultrasound images are consistently darker because the lengthwise scan window intentionally starts before the cell height to ensure full coverage and therefore overlaps the cell holder. In this overlap region, the acoustic path intersects fixture components, introducing additional attenuation and scattering unrelated to the internal cell structure. This effect appears in both through-transmission and reflection, so these rows are treated as a fixture margin and are not interpreted in the analysis.

To facilitate visual interpretation, all intensity images are displayed after per-image min–max normalization to their own dynamic range. This choice accentuates spatial contrast and makes subtle structures more apparent. As a consequence, the displayed values are unitless and each panel has its own scale, so pixel intensities cannot be compared quantitatively across images. Cross-condition comparisons should therefore rely on analyses expressly designed for that purpose (e.g., orientation-difference maps or reported summary statistics), rather than on raw color levels.

3. Results and discussion

3.1. Detecting negative tab position in reflection scans

Across all three cells, the reflection scans exhibit a characteristic, dark, rectangular feature in the unrolled angle–height representation (Marking 1 in Fig. 4a–c). This feature originates at the upper edge of the scan window and extends approximately to mid-height. To make this contrast visible, the per-pixel intensity was computed within a time gate positioned on the later portion of the first front-wall echo, and the resulting image was contrast-stretched.

The reflection images also exhibit a large-scale division into relatively brighter and darker halves (roughly 90–270° versus 270–90°). This asymmetric shading is consistent with a slight off-axis rotation (small eccentricity) of the mounted cell, which produces an angle-dependent sensor–cell standoff distance and thereby modulates the front-wall echo amplitude. We therefore interpret this two-tone background as a geometric artifact rather than a material feature.

To localize the origin of the dark rectangular region, we mapped individual ultrasound rows onto the corresponding CT cross-section. Using the copper orientation marker in the CT to define the angular zero and the known start angle of the ultrasound acquisition, the co-registration reveals that the dark region coincides with the negative tab, which in all three cells lies very close to the can wall (Fig. 4 right side). The axial extent of the dark rectangle matches the tab's vertical length in the CT overlays. This is shown in the supplementary material (S2).

Apart from the tab-associated sector, the reflection images appear mostly homogeneous. This homogeneity indicates that the time gate on the late part of the first reflection predominantly probes the can wall and its immediate vicinity. These reflections results from a large difference in acoustic impedance between the silicone oil and the cell wall as described in Eqs. (1) and (2).

Nevertheless, we observe persistent, approximately circular, localized contrast features at specific coordinates (Fig. 4(a) Marking 2, (b) Marking 2 and 3, (c) Marking 2). Although they do not coincide with obvious blemishes on the outer can surface, their stability across rotations and repeated scans argues against an acquisition artifact. Example time series of dark and bright pixels with the corresponding time gates are shown in the supplementary material (S1).

Fig. 5 plots the intensity curves at 20 mm and 50 mm for each cell. The x axis is again the angle and the y axis depicts the intensity. The Tab differences are Cell 1: 6.97e+09, Cell 2: 4.44e+09 and Cell 3: 4.84e+09.

To investigate the sensitivity of the gate boundaries, we generated intensity images with a +/− 20% shifted gate start t_0 and normalized them with the minimal and maximal values in these images. We chose to keep the gate end fixed, because it is positioned after the first echo were the amplitude is close to 0 and does not change until the second echo arrives. The sensitivity analysis revealed a mean change of 22.8% per pixel for a positive shift and a 8.53% change for a negative shift. Even though these percentages are high, looking at the images shows that the structure of the image (e.g. tab position) are not effected by these changes. The images are shown in the supplementary material S9.

3.2. Detecting electrolyte motion in through transmissions

The images in this subsection are through-transmission intensity maps constructed from the onset of the received waveform. For each angular and axial position, the intensity is computed within a short gate at the beginning of the first arrival so as to emphasize the direct through-path while suppressing contributions from internal reverberations and circumferential/creeping waves. These gated first-arrival signals do not exhibit a dominant 1 MHz component. Instead, a substantial fraction of the energy lies around 200 kHz, consistent with excitation of the transducer's second mode and with the cell acting as a strong high-frequency attenuator. We therefore interpret the resulting intensity maps as being governed primarily by lower-frequency content that is less damped by the cell.

To investigate the sensitivity of the gate boundaries, we generated intensity images with a +/− 20% shifted gate end t_1 and normalized them with the minimal and maximal values in these images. We chose to keep the gate start fixed, because it is positioned before the signal arrives. The sensitivity analysis revealed a mean change of 12.37% per

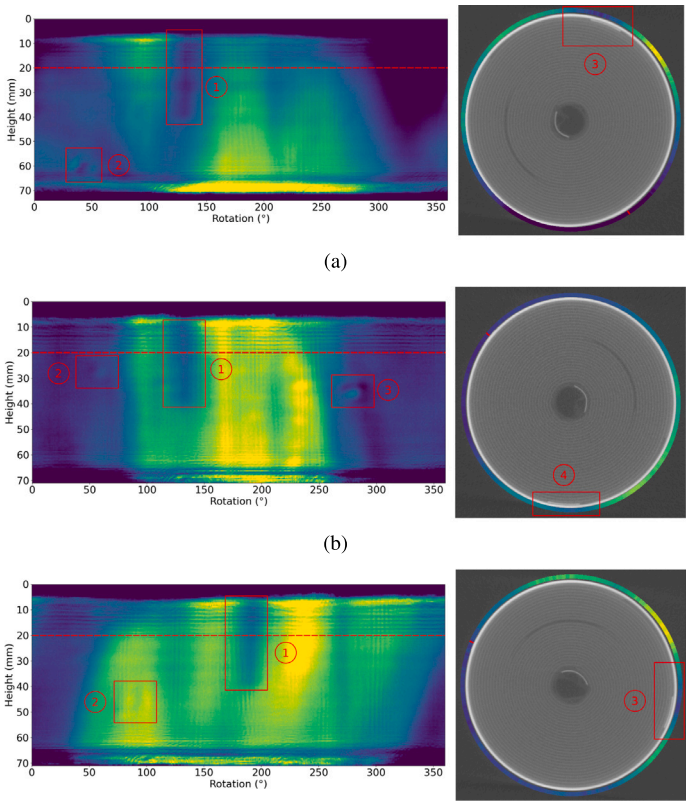

Fig. 4. Detecting negative tab position in reflection scans. The negative tab is visible as rectangular dark spot in reflection scans of all three measured cells and marked in each image with Marking 1. Right side shows the row at height 20 mm (indicated by a red horizontal line on the left) mapped to the corresponding CT slice to show that the angular orientation of the dark spot matches the tab position. The red spot on the ultrasound circle indicates 0° in the unrolled image. **(a):** Cell 1. **(b):** Cell 2. **(c):** Cell 3.

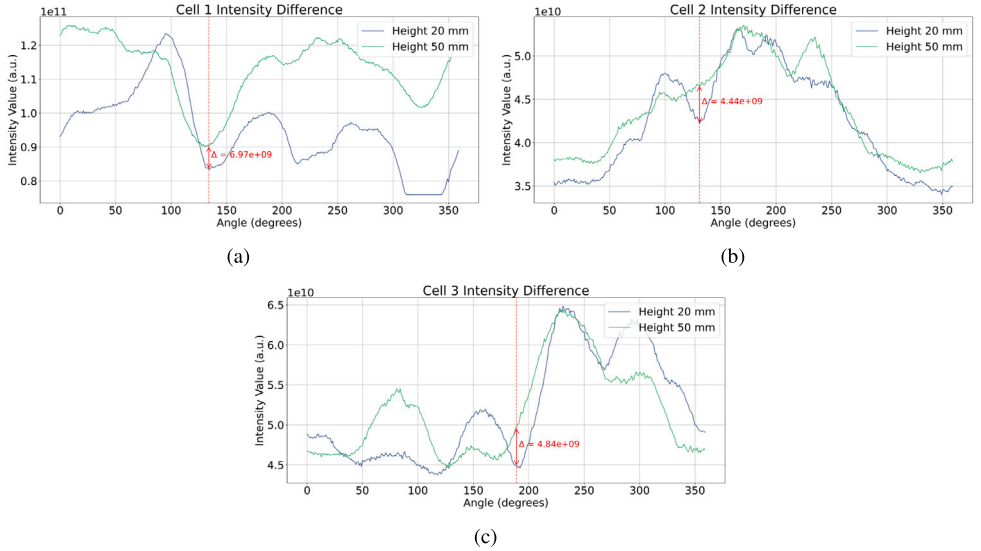

Fig. 5. Comparing intensity curves at height 20 mm, which includes the tab, with curves at height 50 mm, which does not include the tab. **(a):** Cell 1. **(b):** Cell 2. **(c):** Cell 3.

pixel for a negative shift and a 93.47% change for a positive shift. The images are shown in S10.

To probe gravity-driven effects, each cell was scanned in two orientations, with the negative tab facing downward (NT-down) and with it facing upward (NT-up). To minimize any position-induced differences, the entire scanner assembly was rotated in the silicone oil bath between acquisitions so that the transducer–cell geometry remained unchanged relative to the rig. As a result, the negative tab appears at the top edge of every image. A consistency check using reflection images from both orientations was performed and showed no significant misalignment, indicating that differences observed in the through images were not due to repositioning.

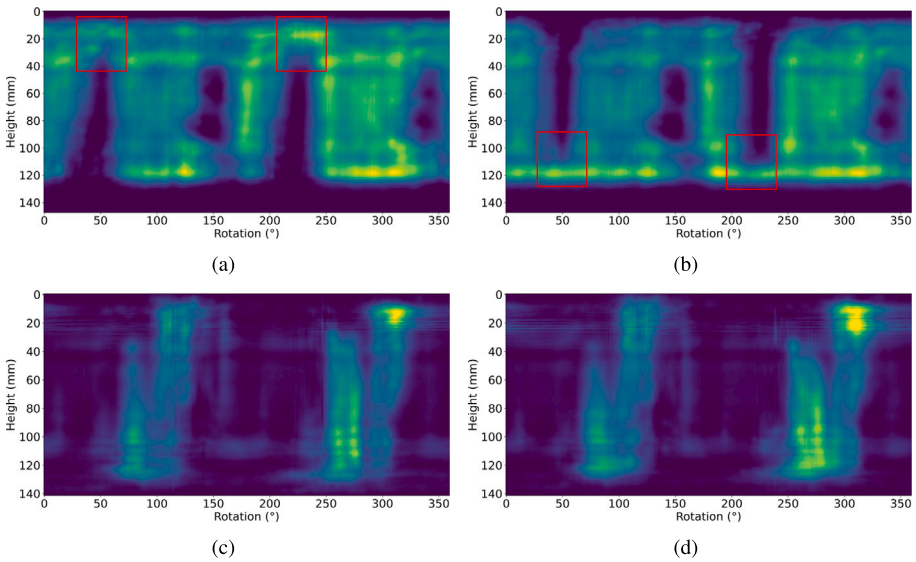

Fig. 6. Intensity images of Cell 1 for transmission measurements in different orientations. The red squares in a and b show areas with the largest difference for the different orientations. **(a):** Image with negative tab facing downward (4.2 V). **(b):** Image with negative tab facing upward (4.2 V). **(c):** Image with negative tab facing downward (3.5 V). **(d):** Image with negative tab facing upward (3.5 V)

The through-transmission intensity maps for Cell 1 at 4.2 V and 3.5 V are shown in Fig. 6. At 4.2 V (Figs. 6a and b), the red squares highlight regions with the largest intensity differences between the two orientations (negative tab up vs. down), indicating a strong orientation-dependent effect in a localized angular sector. The intensity increased at the side that faces gravity, which suggests that the electrolyte reservoir is responsible for the increase. In contrast, at 3.5 V (Figs. 6c and d), the corresponding images do not exhibit such pronounced orientation-induced changes. Beyond these orientation effects, the 4.2 V and 3.5 V images also differ markedly from each other in their overall intensity patterns, independent of orientation, suggesting a strong, spatially localized dependence of the acoustic response on state of charge. A detailed analysis of this SoC-dependent contrast is beyond the scope of the present work, in which we deliberately focus on the dominant contribution of electrolyte redistribution. Example time series of dark and bright pixels with the corresponding time gates are shown in the supplementary material S1.

For a direct, pixel-wise comparison between orientations, we computed difference maps between the two through-transmission images (Fig. 7). For each pixel, the difference is defined as the intensity in the NT-down orientation minus the intensity in the NT-up orientation. Positive differences (NT-down higher) are shown in red, negative differences (NT-up higher) in blue, and values close to zero appear near white. For each cell, the 4.2 V map is normalized by its own maximum absolute difference. The corresponding 3.5 V map is normalized by the same maximum absolute difference as the 4.2 V map of that cell, allowing a direct visual comparison of the relative magnitude of orientation-induced changes between states of charge. At 4.2 V (left panels in Fig. 7), the difference maps retain the overall 180° periodicity expected from the transmission geometry, similar to the aluminum reference dummy. All three cells exhibit a pronounced vertical band of large positive or negative differences that spans almost the full height and repeats after 180°, indicating a strong orientation dependence in a narrow angular sector. Outside this band, the differences are small, showing that the direct-path transmission is nearly identical between NT-down and NT-up in the remaining angular range. Given that the only change between the two acquisitions is the orientation of the fully charged cell with respect to gravity, these strong, localized orientation effects are consistent with a gravity-driven redistribution of mobile electrolyte at high SoC. This interpretation is supported by the CT observations at 4.2 V, which show a central electrolyte reservoir that can shift with orientation.

It is important to note that the cell is not perfectly symmetric because the top and bottom end caps differ. The positive side includes a cap stack with the current interrupt device and crimp, whereas the negative side is a comparatively simple base. This asymmetry influences the bulk electrolyte distribution and the way a gravity-driven electrolyte pool forms and moves. As a result, the NT-down and NT-up images, and hence their difference maps, are not expected to form exact mirror pairs.

At 3.5 V (right panels in Fig. 7), the same difference-map construction and normalization are used. Compared to 4.2 V, the magnitude and extent of the orientation-induced differences are much smaller: the high-amplitude vertical band largely disappears, and most pixels remain close to zero (white) across angle and height. This reduced sensitivity to orientation is in line with the CT findings at 3.5 V, where no bulk electrolyte pool is present in the central hole. Nevertheless, small residual red and blue patches remain, suggesting that more subtle electrolyte redistributions or local wetting changes, although no longer forming a macroscopic reservoir, still produce measurable but weaker modulations of the early through-path transmission at low frequencies. Across all three cells, the summed differences between the NT-down and NT-up images decrease strongly when going from 4.2 V to 3.5 V. For Cell 1, the total orientation-induced change at 3.5 V is only about one fifth of that at 4.2 V, corresponding to a reduction of roughly 82%. For Cell 2, the change drops to about one sixth of the 4.2 V value (around 85% reduction), and for Cell A3 it is reduced to only a few percent of the high-SoC value (about 94% reduction). These percentages confirm that the strong orientation dependence seen in the difference maps is predominantly a high-SoC phenomenon, whereas at 3.5 V only much weaker residual orientation effects remain.

To further relate through-transmission contrast to internal geometry, we mapped a single through-transmission row onto CT cross-sections, analogous to the registration procedure used in Section 3.1. Specifically, for each cell, we selected a height of 55 mm (near the middle row of the unrolled image) and acquired the data in NT-up orientation to minimize electrolyte interference. The overlays in Fig. 8a–c are rotated such that the negative tab is at the top edge (12 o'clock) of each image and are highlighted with a red arrow, enabling a common angular reference across cells.

CT cross-sections show that the relative positions of the tabs within the jelly roll vary between cells, consistent with production variation. Despite these differences, a common pattern is observed. A pronounced

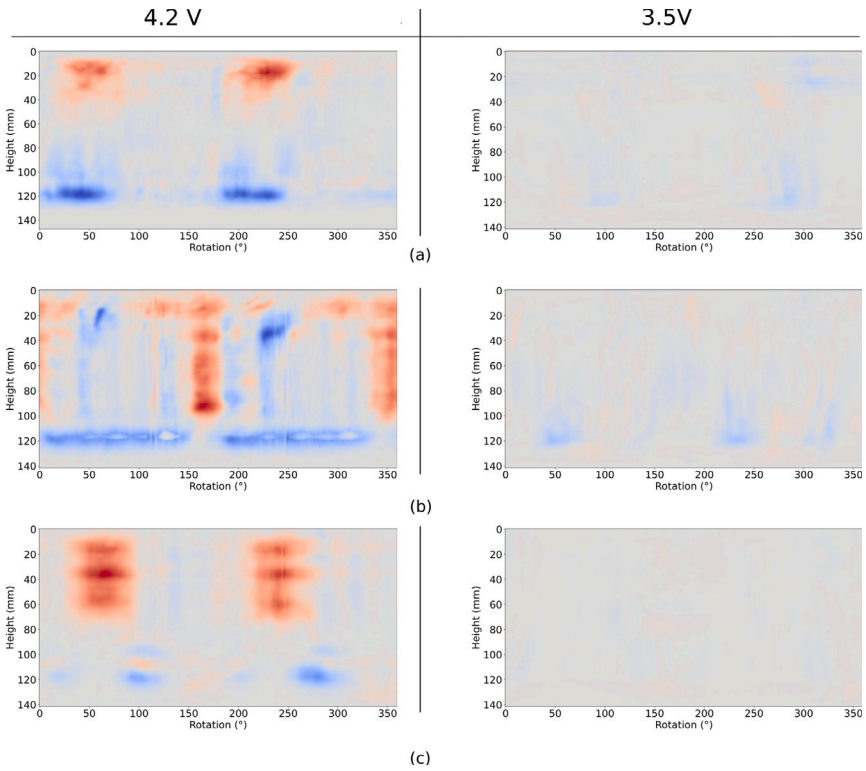

Fig. 7. Detecting electrolyte motion for three different cells by subtracting two through transmission images in two opposite vertical orientations. The colors represent the percentage change relative to the maximum intensity value. Blue signifies high intensity in NT-up orientation and red in NT-down orientation. Left side shows cells at 4.2 V were a large electrolyte reservoir is built up in the middle of the cell which exerts a large influence on the measured intensity. Right side shows images at 3.5 V were the orientation change induces much smaller differences in the measured intensity. **(a):** Cell 1. **(b):** Cell 2. **(c):** Cell 3.

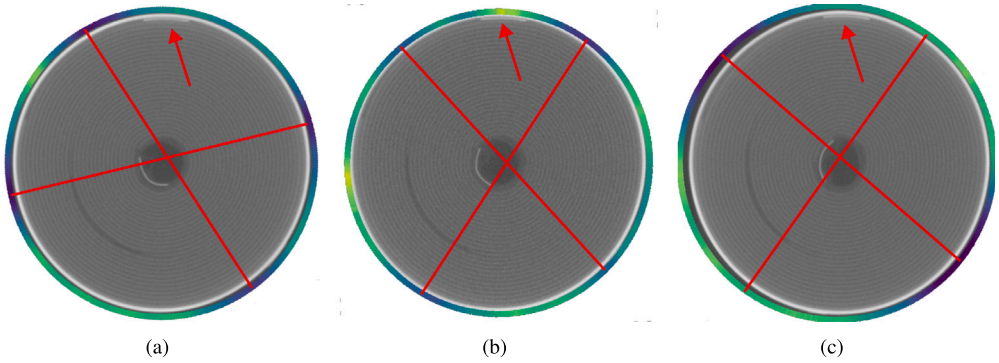

Fig. 8. Ultrasound through transmission image row mapped on CT cross section for 3 cells at height 55 mm. CT images show different tab positions due to manufacturing variation. Dark ultrasound intensity regions coincide with a transmission path through the cell that does not intersect any tabs. Opposing dark regions are highlighted with a red line and the outer negative tab is highlighted with a red arrow **(a):** Cell 1. **(b):** Cell 2. **(c):** Cell 3.

dark, low-intensity column appears at an angle approximately 15° counterclockwise from the negative tab, and a second column lies roughly 90° clockwise from the first. The second column is less visible for Cell 3. By symmetry of the through path, both columns repeat after 180°. The dark spots and the 180° counterparts are highlighted with red lines in Fig. 8. The first attenuation column aligns with a direct acoustic path that does not intersect with the current collector tabs closer to the can wall. One possible interpretation is that these tabs locally increase radial pressure [34] within the wound layers, improving interlayer contact and thereby strengthening acoustic coupling, whereas paths that bypass tabbed sectors experience slightly poorer coupling and thus reduced transmitted amplitude, producing the observed dark columns.

We emphasize that this mechanistic explanation is a working hypothesis rather than a proven causality. The main supporting evidence is that (i) the attenuation columns are stable across repeated scans and across all three cells, (ii) their angular positions are reproducible relative to the negative tab despite variations, and (iii) they do not coincide with obvious features on the outer can or fixture. However, our current CT data do not resolve small variations in local compression or density along these paths, and no mechanical modeling has been performed. A definitive test would require combining ultrasound with high-resolution CT under controlled mechanical loading and/or electro-mechanical simulations of the wound stack, which is beyond the scope of this work.

4. Conclusion

This work presents a compact rotational ultrasound scanner tailored to cylindrical Li-ion cells that acquires two-dimensional angle–height images in through-transmission and reflection with two opposing single-element transducers. Selective time gating of the first arrival in transmission suppresses creeping and circumferential waves and restores interpretable contrast. In reflection measurements, placing the time gate on the later portion of the first front-wall enhances the visibility of tab-associated sectors. Co-registration with X-ray CT via an external angular marker links acoustic features to internal structures and enables direct mapping to tab positions.

Validation on a machined aluminum dummy confirms accurate image formation and highlights the importance of time gating for cylindrical specimens. Applied to three 26650 cells, reflection-mode imaging robustly reveals the negative tab as a dark rectangular sector with correct angular and axial extent. Early-gated transmission, dominated by lower-frequency content near 200 kHz, captures gravity-driven electrolyte redistribution at full state of charge as orientation-dependent vertical bands. At lower state of charge, the orientation effect diminishes but remains detectable, and when electrolyte effects are minimized, stable attenuation columns appear at reproducible angles relative to the negative tab, which we hypothesize may be linked to local mechanical constraints influencing acoustic coupling.

These results demonstrate that rotational, gated ultrasound imaging can deliver interpretable spatial contrast in cylindrical cells without phased arrays and that transmission and reflection provide complementary sensitivity to bulk coupling and near-surface boundary conditions. The approach offers practical routes for non-destructive tab localization, screening of electrolyte wetting and pooling, and inference of internal mechanical conditions that affect interlayer contact, while the use of single-element transducers and rotational motion keeps hardware complexity low.

Several limitations of the present study should be acknowledged, which also point to concrete directions for future work:

- **Low-frequency dominance and spatial resolution.** Although 1 MHz transducers were used, strong attenuation in the wound electrode stack means that the effective transmitted signal is dominated by the second mode around 200 kHz. This low frequency content limits depth and lateral resolution and prevents resolving individual layers. Future work should explore transducers with tailored bandwidth and center frequencies
- **CT–ultrasound co-registration accuracy.** Co-registration between CT and ultrasound is presently based on an external copper strip and manual alignment of the marked angular position in the scanner. As discussed in Section 3.1, this yields an angular uncertainty, which is sufficient for the large-scale features studied here (tabs, electrolyte bands) but limits fully quantitative comparisons. Future work should focus on improving registration by using integrated fiducial markers, more precise mechanical indexing of the cell in both CT and ultrasound fixtures, and automated image-based registration algorithms to reduce these uncertainties.
- **Sample diversity and operating conditions.** The study is limited to three new 26650 cells of one commercial type and ex-situ measurements at room temperature and static states of charge. The generality of the observed tab signatures, electrolyte-redistribution bands, and mechanically induced attenuation features remains to be established across chemistries, form factors, and ageing states. Future work should therefore extend the approach to larger formats such as 4680 cells, different chemistries and manufacturers.
- **State-of-charge dependence beyond electrolyte effects.** In this work, state of charge was varied deliberately only between conditions that induce pronounced bulk electrolyte motion (e.g., 3.5 V vs. 4.2 V), in order to isolate and interpret the dominant contribution of electrolyte redistribution. We did not systematically investigate SoC-induced changes in elastic properties, lithiation gradients, or local mechanical stress that may also affect ultrasound signals. Future studies should perform finer SoC sweeps with controlled rest times, combine ultrasound with electrochemical and mechanical modeling, and correlate multi-SoC ultrasound data with CT or other imaging to disentangle electrolyte-related contrast from purely mechanical or compositional SoC effects.

CRediT authorship contribution statement

Tobias Röhmel: Writing – review & editing, Writing – original draft, Visualization, Validation, Supervision, Software, Resources, Project administration, Methodology, Investigation, Funding acquisition, Formal analysis, Data curation, Conceptualization. **Morian Sonnet:** Writing – review & editing, Methodology, Formal analysis. **Gereon Stahl:** Writing – review & editing, Methodology, Formal analysis. **Duc Minh Nguyen:** Writing – review & editing. **Tim Falkenstein:** Writing – review & editing, Conceptualization. **Dirk Uwe Sauer:** Supervision, Funding acquisition.

Declaration of Generative AI and AI-assisted technologies in the writing process

During the preparation of the manuscript the authors used GPT5/OpenAI in order to improve readability and language. After using this tool, the authors reviewed and edited the content as needed and take full responsibility for the content of the publication.

Declaration of competing interest

The authors declare that they have no known competing financial interests or personal relationships that could have appeared to influence the work reported in this paper.

Acknowledgments

The authors gratefully acknowledge the financial support by the Federal Ministry of Education and Research, Germany through the project DORSMAN (BMBF 03XP0633B). Open Access funding enabled and organized by Projekt DEAL.

Appendix A. Supplementary data

Supplementary material related to this article can be found online at https://doi.org/10.1016/j.jpowsour.2026.239455.

Data availability

Data will be made available on request.

References

[1] C. Gervillié-Mouravieff, W. Bao, D.A. Steingart, Y.S. Meng, Non-destructive characterization techniques for battery performance and life-cycle assessment, Nat. Rev. Electr. Eng. 1 (8) (2024) 547–558, http://dx.doi.org/10.1038/s44287-024-00069-y, Publisher: Nature Publishing Group. URL https://www.nature.com/articles/s44287-024-00069-y.

[2] H. Pegel, D. Wycisk, A. Scheible, L. Tendera, A. Latz, D.U. Sauer, Fast-charging performance and optimal thermal management of large-format full-tab cylindrical lithium-ion cells under varying environmental conditions, J. Power Sources 556 (2023) 232408, http://dx.doi.org/10.1016/j.jpowsour.2022.232408, URL https://www.sciencedirect.com/science/article/pii/S0378775322013854.

[3] LG Energy Solution to Exclusively Supply Cylindrical Batteries for Aptera's Solar Electric Vehicles - LG Energy Solution, 2025, URL https://news.lgensol.com/company-news/press-releases/3501/.

[4] Panasonic Energy Ready to Commence Mass Production of 4680 Automotive Lithium-ion Batteries | Automotive Equipment | Products & Solutions | Press Releases, 2024, URL https://news.panasonic.com/global/press/en240909-7,

[5] Potentials of 46 mm cylindrical cells: On the way to the new standard format, 2023, URL https://www.isi.fraunhofer.de/en/blog/themen/batterie-update/46-mm-rundzellen-potenziale-standardformat-batteriezellen.html.

[6] Charge faster, drive further: BMW Group reveals revolutionary electric drive concept with 800 V technology for the Neue Klasse, 2025, URL https://www.press.bmwgroup.com/global/article/detail/T0448099EN/charge-faster-drive-further:-bmw-group-reveals-revolutionary-electric-drive-concept-with-800v-technology-for-the-neue-klasse?language=en.

[7] K. Tsuruta, M.E. Dermer, R. Dhiman, Cell with a tabless electrode, 2023, URL https://patents.google.com/patent/US11749842B2/en.

[8] S. Baazouzi, N. Feistel, J. Wanner, I. Landwehr, A. Fill, K.P. Birke, Design, Properties, and Manufacturing of Cylindrical Li-Ion Battery Cells—A Generic Overview, Batteries 9 (6) (2023) 309, http://dx.doi.org/10.3390/batteries9060309, Publisher: Multidisciplinary Digital Publishing Institute. URL https://www.mdpi.com/2313-0105/9/6/309.

[9] A.J. Ilott, M. Mohammadi, H.J. Chang, C.P. Grey, A. Jerschow, Real-time 3D imaging of microstructure growth in battery cells using indirect MRI, Proc. Natl. Acad. Sci. 113 (39) (2016) 10779–10784, http://dx.doi.org/10.1073/pnas.1607903113, Company: National Academy of Sciences Distributor: National Academy of Sciences ISBN: 9781607903116 Institution: National Academy of Sciences Label: National Academy of Sciences Publisher: Proceedings of the National Academy of Sciences. URL https://www.pnas.org/doi/abs/10.1073/pnas.1607903113.

[10] S. Chandrashekar, N.M. Trease, H.J. Chang, L.-S. Du, C.P. Grey, A. Jerschow, 7Li MRI of Li batteries reveals location of microstructural lithium, Nat. Mater. 11 (4) (2012) 311–315, http://dx.doi.org/10.1038/nmat3246, Publisher: Nature Publishing Group. URL https://www.nature.com/articles/nmat3246.

[11] J.B. Habedank, F.J. Günter, N. Billot, R. Gilles, T. Neuwirth, G. Reinhart, M.F. Zaeh, Rapid electrolyte wetting of lithium-ion batteries containing laser structured electrodes: in situ visualization by neutron radiography, Int. J. Adv. Manuf. Technol. 102 (9) (2019) 2769–2778, http://dx.doi.org/10.1007/s00170-019-03347-4, URL https://doi.org/10.1007/s00170-019-03347-4.

[12] J.B. Robinson, E. Engebretsen, D.P. Finegan, J. Darr, G. Hinds, P.R. Shearing, D.J.L. Brett, Detection of Internal Defects in Lithium-Ion Batteries Using Lock-in Thermography, ECS Electrochem. Lett. 4 (9) (2015) A106, http://dx.doi.org/10.1149/2.0071509eel, Publisher: IOP Publishing. URL https://iopscience.iop.org/article/10.1149/2.0071509eel/meta.

[13] Q. Wu, L. Yang, N. Li, Y. Chen, Q. Wang, W.-L. Song, X. Feng, Y. Wei, H.-S. Chen, In-situ thermography revealing the evolution of internal short circuit of lithium-ion batteries, J. Power Sources 540 (2022) 231602, http://dx.doi.org/10.1016/j.jpowsour.2022.231602, URL https://www.sciencedirect.com/science/article/pii/S037877532200605X.

[14] D. Wasylowski, H. Ditler, M. Sonnet, T. Falkenstein, L. Leogrande, E. Ronge, A. Blömeke, A. Würsig, F. Ringbeck, D.U. Sauer, Operando visualisation of lithium plating by ultrasound imaging of battery cells, Nat. Commun. 15 (1) (2024) 10237, http://dx.doi.org/10.1038/s41467-024-54319-6, Publisher: Nature Publishing Group. URL https://www.nature.com/articles/s41467-024-54319-6.

[15] L.P. Bauermann, L.V. Mesquita, C. Bischoff, M. Drews, O. Fitz, A. Heuer, D. Biro, Scanning acoustic microscopy as a non-destructive imaging tool to localize defects inside battery cells, J. Power Sources Adv. 6 (2020) 100035, http://dx.doi.org/10.1016/j.powera.2020.100035, URL https://www.sciencedirect.com/science/article/pii/S2666248520300354.

[16] D. Wasylowski, N. Kisseler, H. Ditler, M. Sonnet, G. Fuchs, F. Ringbeck, D.U. Sauer, Spatially resolving lithium-ion battery aging by open-hardware scanning acoustic imaging, J. Power Sources 521 (2022) 230825, http://dx.doi.org/10.1016/j.jpowsour.2021.230825, URL https://www.sciencedirect.com/science/article/pii/S0378775321013136.

[17] A.G. Hsieh, S. Bhadra, B.J. Hertzberg, P.J. Gjeltema, A. Goy, J.W. Fleischer, D.A. Steingart, Electrochemical-acoustic time of flight: in operando correlation of physical dynamics with battery charge and health, Energy Environ. Sci. 8 (5) (2015) 1569–1577, http://dx.doi.org/10.1039/C5EE00111K, Publisher: The Royal Society of Chemistry. URL https://pubs.rsc.org/en/content/articlelanding/2015/ee/c5ee00111k.

[18] T.D. Nguyen, H. Sun, R. Amin, P. Ramuhalli, C.-B.M. Kweon, I. Belharouak, Ultrasonic Nondestructive Diagnosis of Cylindrical Batteries Under Various Charging Rates, J. Electrochem. Soc. 171 (2) (2024) 020522, http://dx.doi.org/10.1149/1945-7111/ad2642, Publisher: IOP Publishing. URL https://iopscience.iop.org/article/10.1149/1945-7111/ad2642/meta.

[19] S. Montoya-Bedoya, E. Garcia-Tamayo, D. Rohrbach, J.P. Gaviria-Cardona, H.V. Martinez-Tejada, B. Planden, D.A. Howey, W.F. Florez, R.A. Valencia, M. Bernal, Quantitative Ultrasound Spectroscopy for Screening Cylindrical Lithium-Ion Batteries for Second-Life Applications, Batter. & Supercaps 7 (5) (2024) e202400002, http://dx.doi.org/10.1002/batt.202400002, Publisher: John Wiley & Sons, Ltd. URL https://chemistry-europe.onlinelibrary.wiley.com/doi/full/10.1002/batt.202400002.

[20] J. Gao, Y. Lyu, C. He, Estimating State of Charge of Lithium-ion Batteries by Using Ultrasonic Guided Waves Detection Technology, J. Phys.: Conf. Ser. 2198 (1) (2022) 012015, http://dx.doi.org/10.1088/1742-6596/2198/1/012015, Publisher: IOP Publishing. URL https://iopscience.iop.org/article/10.1088/1742-6596/2198/1/012015/meta.

[21] Y. Cheng, S. Zhao, G. Shen, S. Zhang, P. Yao, Real-Time Temperature Monitoring of Lithium Batteries Based on Ultrasonic Technology, ACS Omega 9 (17) (2024) 19517, http://dx.doi.org/10.1021/acsomega.4c00983, URL https://pmc.ncbi.nlm.nih.gov/articles/PMC11064029/.

[22] Y. Tian, S. Yang, R. Zhang, J. Tian, X. Li, State of charge estimation of lithium-ion batteries based on ultrasonic guided waves by chirped signal excitation, J. Energy Storage 84 (2024) 110897, http://dx.doi.org/10.1016/j.est.2024.110897, URL https://www.sciencedirect.com/science/article/pii/S2352152X2400481X.

[23] Z. Huang, Y. Zhou, Z. Deng, K. Huang, M. Xu, Y. Shen, Y. Huang, Precise State-of-Charge Mapping via Deep Learning on Ultrasonic Transmission Signals for Lithium-Ion Batteries, ACS Appl. Mater. Interfaces (2023) http://dx.doi.org/10.1021/acsami.2c22210, Publisher: American Chemical Society. URL https://pubs.acs.org/doi/full/10.1021/acsami.2c22210.

[24] L. Gold, T. Bach, W. Virsik, A. Schmitt, J. Müller, T.E.M. Staab, G. Sextl, Probing lithium-ion batteries' state-of-charge using ultrasonic transmission – Concept and laboratory testing, J. Power Sources 343 (2017) 536–544, http://dx.doi.org/10.1016/j.jpowsour.2017.01.090, URL https://www.sciencedirect.com/science/article/pii/S0378775317301003.

[25] R.J. Copley, R.S. Dwyer-Joyce, Prediction of the internal structure of a lithium-ion battery using a single ultrasound wave response, J. Energy Storage 72, Part E (2023) Publisher: Elsevier BV. URL https://eprints.whiterose.ac.uk/id/eprint/203538/.

[26] P.-S. Ma, H. Lee, Y.-H. Seo, Identifying ultrasonic scattering from multi-layered lithium-ion battery cells: Mechanical modeling and experimental validation, J. Energy Storage 92 (2024) 112077, http://dx.doi.org/10.1016/j.est.2024.112077, URL https://www.sciencedirect.com/science/article/pii/S2352152X24016633.

[27] H. Li, Z. Zhou, Numerical Simulation and Experimental Study of Fluid-Solid Coupling-Based Air-Coupled Ultrasonic Detection of Stomata Defect of Lithium-Ion Battery, Sensors 19 (10) (2019) 2391, http://dx.doi.org/10.3390/s19102391, Publisher: Multidisciplinary Digital Publishing Institute. URL https://www.mdpi.com/1424-8220/19/10/2391.

[28] B. Zhang, Y. Lyu, J. Gao, G. Song, Y. Zheng, Y.-c. Lee, C. He, Ultrasonic characterization of multi-layered porous lithium-ion battery structure for state of charge, Ultrasonics 134 (2023) 107060, http://dx.doi.org/10.1016/j.ultras.2023.107060, URL https://www.sciencedirect.com/science/article/pii/S0041624X23001361.

[29] J. Gaviria-Cardona, M. Guzman-De Las Salas, N. Montoya-Escobar, W. Florez-Escobar, R. Valencia-Cardona, H.V. Martinez, Ultrasound simulation technique as state-of-health estimation method of lithium-ion batteries, in: 2021 IEEE UFFC Latin America Ultrasonics Symposium (LAUS), 2021, pp. 1–4, http://dx.doi.org/10.1109/LAUS53676.2021.9639223, URL https://ieeexplore.ieee.org/abstract/document/9639223.

[30] S. Solchenbach, C. Tacconis, A.G. Martin, V. Peters, L. Wallisch, A. Stanke, J. Hofer, D. Renz, B. Lewerich, G. Bauer, M. Wichmann, D. Goldbach, A. Adam, M. Spielbauer, P. Lamp, J. Wandt, Electrolyte motion induced salt inhomogeneity – a novel aging mechanism in large-format lithium-ion cells, Energy & Environ. Sci. 17 (19) (2024) 7294–7317, http://dx.doi.org/10.1039/D4EE03211J, Publisher: Royal Society of Chemistry. URL https://pubs.rsc.org/en/content/articlelanding/2024/ee/d4ee03211j.

[31] Z. Deng, Z. Huang, Y. Shen, Y. Huang, H. Ding, A. Luscombe, M. Johnson, J.E. Harlow, R. Gauthier, J.R. Dahn, Ultrasonic Scanning to Observe Wetting and "Unwetting" in Li-Ion Pouch Cells, Joule 4 (9) (2020) 2017–2029, http://dx.doi.org/10.1016/j.joule.2020.07.014, URL https://www.sciencedirect.com/science/article/pii/S2542435120303329.

[32] T. Röhmel, ISEA / Roundcellscanner-CAD · GitLab, 2025, URL https://git.rwth-aachen.de/isea/roundcellscanner-cad,

[33] MarlinFirmware/Marlin, 2025, original-date: 2011-08-13T08:07:20Z. URL https://github.com/MarlinFirmware/Marlin.

[34] W. Jiang, H. Li, S. Wang, S. Wang, W. Wang, Dynamic Volumography of Cylindrical Li-Ion Battery Cells by Watching Its Breath During Cycling, CCS Chem. 5 (6) (2023) 1308–1317, http://dx.doi.org/10.31635/ccschem.023.202202680, Publisher: Chinese Chemical Society. URL https://www.chinesechemsoc.org/doi/10.31635/ccschem.023.202202680.